Polarization discrimination technique to maximize LIDAR signal-to-noise ratio for daylight operations

Yasser Y. Hassebo, Barry Gross, Min Oo, Fred Moshary, and Samir Ahmed

Optical Remote Sensing Laboratory - The City College of the City University of New York

Convent Ave. & 140 St., New York, NY 10031, USA

E-mail: ahmed@ccny.cuny.edu

Abstract

The impact and potential of a polarization selection technique to reduce sky background signal for linearly polarized monostatic elastic backscatter lidar measurements are examined. Taking advantage of naturally occurring polarization properties in scattered sky light, we devised a polarization discrimination technique in which both the lidar transmitter and receiver track and minimize detected sky background noise while maintaining maximum lidar signal throughput. Lidar elastic backscatter measurements, carried out continuously during daylight hours at 532 nm show as much as a factor of $\sqrt{10}$ improvement in signal-to-noise ratio over conventional un-polarized schemes. For vertically pointing lidars, the largest improvements, are limited to the early morning and late afternoon hours, while for non-vertical scanning lidars, significant improvements are achievable over more extended time periods with the specific times and improvement factors depending on the specific angle between the lidar and solar axes. The resulting diurnal variations in SNR improvement sometimes show asymmetry with solar angle,

which analysis indicates can be attributed to changes in observed relative humidity that modifies the underlying aerosol microphysics and observed optical depth.

OCIS codes 280.3640; 280.0280; 280.1100;

1. Introduction

Polarization selective lidar systems have been used primarily for separating and analyzing polarization of lidar returns, for a variety of purposes, including examination of multiple scattering effects and for differentiating between different atmospheric scatterers and aerosols.[1-9] In the approach described here, the polarized nature of the sky background light is used to devise a polarization selective scheme to reduce the sky background power detected in a lidar. This leads to improved signal-to-noise ratios and attainable lidar ranges, which are important considerations in daylight lidar operation.[10-11]

The approach discussed here is based on the fact that most of the energy in linearly polarized elastically backscattered lidar signals retains the transmitted polarization[1,6,9] , while the received sky background power (P_b) observed by the lidar receiver shows polarization characteristics that depend on both the angle between the direction of the lidar and the direct sunlight, as well as the orientation of the detector polarization to the scattering plane. In particular, the sky background signal is minimized in the plane perpendicular to the scattering plane, while the difference between the in-plane component and the perpendicular components (i.e degree of polarization) depends solely on the scattering angle.

For a vertically pointing lidar, the scattering angle is simply the solar zenith angle (see Figure 1). The degree of polarization of sky background signal observed by the lidar is largest for solar zenith angles near $\theta_S \approx 90^o$ and smallest at solar noon. The essence of the proposed approach is therefore, at any time, to first determine the parallel component of P_b with a polarizing analyzer on the receiver, thus minimizing the detected P_b, and then orienting the polarization of the outgoing lidar signal so that the polarization of the received lidar backscatter signal is aligned with the receiver polarizing analyzer. This ensures unhindered passage of the primary lidar backscatter returns, while at the same time minimizing the received sky background P_b , and thus maximizing both SNR and attainable lidar ranges.

The experimental approach and system geometry to implement the polarization discrimination scheme are described in Section 2. Section 3 presents results of elastic lidar backscatter measurements for a vertically pointing lidar at 532 nm taken on a clear day in the New York City urban atmosphere, that examine the range of application of the technique. In particular, the diurnal variations in P_b as functions of different solar angles are given and the SNR improvement is shown to be consistent with the results predicted from the measured degree of linear polarization, with maximum improvement restricted to the early morning and late afternoon. Section 4 examines the situations in which asymmetric diurnal variations in sky P_b are observed, and analyses the possibility that an increase in relative humidity (RH), consistent with measured increases in measured precipitable water vapor (PWV) and aerosol optical depth (AOD), may account for the asymmetry.

Analysis of the overall results is presented in Section 5, where the SNR improvement factor is compared with a single scattering radiative transfer theory. Possible modifications due to multiple scattering are also explored. In Section 6, the diurnal variation of the polarization

rotation angle is compared to the theoretical result and an approach for automation of the technique based on theory is discussed. In addition, the potential impact of the method on non-vertical scanning lidar systems is examined and shown to have a much wider range of effective operational periods during the day compared to vertical lidars. Conclusions and summary are presented in Section 7.

2. Experimental approach and System geometry

The City University of New York (CUNY) has developed two ground-based lidar systems, one mobile and one stationary, that operate at multiple wavelengths for monostatic elastic backscatter retrievals of aerosol and cloud characteristics and profiles. Lidar measurements are performed at the Remote Sensing Laboratory of the City College of New York, (CCNY). The lidar systems are designed to monitor enhanced aerosol events as they traverse the eastern coast of the United States, and form part of NOAA's Cooperative Remote Sensing Center (CREST) Regional East Atmospheric Lidar Mesonet (REALM) lidar network. The lidar measurements reported here were carried out with the mobile elastic monostatic biaxial backscatter lidar system at the CCNY site (longitude 73.94 W, latitude 40.83 N), at 532 nanometers wavelength. The lidar transmitter and the receiver subsystems are detailed in table I. The lidar return from the receiver telescope is detected by a photo-multiplier (PMT R11527P) with a 1 nm bandwidth optical filter (532F02-25 Andover), centered at the 532 nm wavelength. For extended ranges, data is acquired in the photon counting (PC) mode, typically averaging 600 pulses over a one minute interval and using a Licel 40-160 transient recorder with 40 MHz sampling rate for A/D conversion and a 250 MHz photon counting sampling interval. Figure 2

shows the arrangement used to implement the polarization-tracking scheme. To select the polarization of light entering the detector, a polarizing beam splitter is located in front of the collimating lens that is used in conjunction with a narrow band filter (alternatively, dichroic material polarizers were also used). This polarizing beam splitter (analyzer) is then rotated to minimize the detected sky background P_b. On the transmission side, a half wave plate at the output of the polarized laser output is then used to rotate the polarization of the outgoing lidar beam so as to align the polarization of the backscattered lidar signal with the receiver polarizing analyzer and hence maximize its throughput (i.e., at the minimum P_b setting). This procedure was repeated for all measurements, with appropriate adjustments being made in receiver polarization analyzer alignment and a corresponding tracking alignment in the transmitted beam polarizations to adjust for different solar angles at different times of the day, and hence minimize the detected P_b and maximize lidar SNR. Cross polarized extinction ratios on the receiver analyzer were approximately 10^{-4}.

3. Results

3.1 *Lidar data*

Figure 3 shows an example of experimental results (6:29 PM 07 October 2004) obtained for different polarization alignments. The upper trace corresponds to the receiver polarization analyzer oriented to minimize P_b and the lidar transmitter polarization oriented to maximize the detected backscattered lidar signal while the lower trace is the result when orthogonal orientations of both receiver analyzer and lidar polarization are used, minimizing the sky background component in the return signal.

Similar results were obtained for 3:00 PM and noon on the same day. Figure 4 shows the resulting return signals in the far zone where the sky background signal is the dominant component (20-30 km range) for these times and for both orthogonal polarizations. The relative impact on the sky background signal, $P_{b,}$ of the polarization discrimination scheme is seen to be largest at 6:29 PM, when the lidar solar angle is large (89°), while at noon it is minimal. Clearly, for each set of measurements, the detected signal for maximum P_b is much noisier than the detected signal with minimum P_b . This is consistent with the shot noise limit applicable to PMT's where the detected noise amplitude (standard deviation) is proportional to the square root of the mean detected background signal. (i.e. $\Delta P \propto \sqrt{\langle P \rangle}$) where P is the detector output, whose mean value is proportional to P_b. This relation has been verified in our experiments and the results summarized in Table II, which confirm that the detector operates in the shot noise limited regime.

In assessing the extent to which the polarization discrimination detection scheme can improve the SNR and the operating range; we compare the detected SNR with a polarizer, to that which would be obtained if no polarization filtering was used. When shot noise from background light is large compared to that from the lidar signal backscatter, the SNR improvement can be expressed in terms of an SNR improvement factor (G_{imp}) expressed in terms of maximum and minimum P_b measurements ($P_b^{\max}, P_b^{\min}$) as:

$$G_{imp} = \frac{SNR_{Max}}{SNR_{Unpol}} = \sqrt{\left(\frac{P_b^{\min} + P_b^{\max}}{P_b^{\min}} \right)} = \sqrt{1 + \left(\frac{P_b^{\max}}{P_b^{\min}} \right)} \quad (1)$$

To examine how the decreased P_b translates into a SNR improvement, we show in Figure 5 the range dependent SNR obtained for both maximum and minimum noise polarization orientations for a representative lidar measurement. The results show that for SNR=10, the

range improvement resulting from polarization discrimination resulted in an increase in lidar operating range from 9.38 km to 12.5km (a 34% improvement). Alternatively, for a given lidar range, say 9 km, the SNR improvement was 250%. Another useful way of looking at the effect of SNR improvement is to note that the SNR improves as the square root of the detector's averaging time. Thus a 250% improvement in SNR is equivalent to reducing the required averaging time by a factor of $(1/2.5)^2$.

3.2 SNR Improvement with respect to solar zenith

The SNR improvement factor (G_{imp})is plotted as a function of the local time, Figure 6a, and the solar zenith angle, Figure 6b. Since the solar zenith angle retraces itself as the sun passes through solar noon, it would be expected that the improvement factor (G_{imp}) would be symmetric before and after the solar noon and depend solely on the solar zenith angle. This symmetry is observed in Figures 6a and 6b for measurements made on 19 February 2005 and is supported by the relatively small changes in optical depth (AOD) values obtained from a collocated shadow band radiometer, (morning $\tau = 0.08$, afternoon $\tau = 0.11$)

4. Effect of Variable Precipitable Water Vapor (PWV) on SNR

Symmetry was, however, not always observed in our experimental results. In Figure 7, we plot G_{imp} as a function of the solar zenith angle for 23 February 2005. Small asymmetries were observed. These appear to be related to changes in humidity, which can modify the

scattering properties and lead to enhanced multiple scattering effects. The results are supported by the variation in PWV shown in Figure 8, obtained from the CCNY Global Positioning System GPS measurements which were processed by the NOAA Forecast Systems Laboratory (FSL)[12] for both the asymmetric data of February and the symmetric data of 19 February 2005. In particular, we note that on 23 February the aerosol optical depth measurements from the shadow band radiometer showing larger proportional changes (morning $\tau = 0.16$ afternoon $\tau = 0.09$) which are consistent with the asymmetry in the PWV with higher optical depths corresponding to high PWV (and RH%) conditions.

In section 5.2, we examine the asymmetric behavior of the SNR in more detail, and show that it can be explained using an aerosol model, which is tuned by the optical depth measurements and takes into account the RH level.

5. Discussion and analysis

To compare qualitatively the extent of P_b polarization observed in our experiments with theoretical estimates, we use a single scattering model of the atmosphere, justified by the relatively small optical depths measured by sky radiometry during the experiments. In this limit, P_b is simply proportional to the diffuse transmission, T, of sunlight through the atmosphere, which takes the form:

$$T_i(\mu;\mu_o) = \frac{\tilde{\omega}}{4(\mu - \mu_o)} P_i^{eff} \left(e^{\frac{-\tau}{\mu}} - e^{\frac{-\tau}{\mu_o}}\right) \qquad \textit{where} \qquad i = 1,2 \tag{2}$$

where i =1,2 for parallel (in plane) and perpendicular (out of plane) polarization respectively, μ_0, μ are direction cosines of the solar and viewing angles, τ is the total optical depth, and $\tilde{\omega}$

is the single-scatter albedo. P_1^{eff} and P_2^{eff} are the effective phase functions for the parallel and perpendicular components corresponding to the minimum P_b and maximum P_b. For a two-component atmosphere consisting of a mixture of aerosol and molecules where (τ_{mol} , τ_{aer}) are the optical depths for molecular and aerosol components. The effective phase functions are then a weighted combination given by:

$$P_i^{eff} = \frac{\tau_{mol} P_i^{mol} + \tau_{aer} P_i^{aer}}{\tau_{mol} + \tau_{aer}} \tag{3}$$

where the total phase functions for the molecular component can be written as:

$$P_{Tot}^{mol} = \frac{3}{4}(1 + \cos^2(\theta)) \tag{4}$$

The molecular optical thickness is obtained from the following empirical formula:

$$\tau_{mol} = C_o \left(\frac{\lambda}{\lambda_o}\right)^{-4} \left[1 + C_1 \left(\frac{\lambda}{\lambda_o}\right)^{-2} + C_2 \left(\frac{\lambda}{\lambda_o}\right)^{-4}\right] \tag{5}$$

where the parameter values are $C_o = 0.09364$, $C_1 = 0.0374$, $C_2 = 0.00142$, and $\lambda_o = 550nm$. [13]

The equivalent effective phase functions for the aerosol components depend on the normalized particulate distribution function used, and are given by:

$$P_i^{aer} = S_i(\theta)\left[\frac{4}{q^2 Q_e}\right] \tag{6}$$

$$S_i(\theta) = \int S_i^{norm}(r,\theta)\,\bar{n}(r)\,dr \tag{7}$$

Here S_i is the scattering function for each polarization, Q_e is the Mie extinction efficiency, which is a function of the normalized size parameter $q = 2\pi a/\lambda$ where a is the particle radius and λ is the wavelength, $\bar{n}(r)$ is the appropriate particle distribution function and S_i^{norm} is the normalized single particle scattering function (for a given polarization).[14-16] Since P_b is

proportional to the diffuse transmission *T*, we obtain from Eq. (2) above, the ratio of the maximum noise $P_b^{\max}$ to the minimum noise $P_b^{\min}$ as:

$$\frac{P_b^{\max}}{P_b^{\min}}(\theta) = \frac{T^{\perp}(\mu;\mu_o)}{T^{ll}(\mu;\mu_o)} = \frac{P_2^{eff}}{P_1^{eff}} \tag{8}$$

from which, the SNR improvement function G_{imp} can be obtained using Eq. (1). To evaluate this expression, the optical depth of both the molecular and aerosol components as well as the respective phase of the scattering function should be known.

5.1 Symmetric data set

In examining the symmetric data set obtained on a clear dry day, it should be noted that due to the fairly small optical thickness on (19 February 2005), particle distributions obtained from Aeronet could not be considered accurate. We therefore used a fine-mode-dominated aerosol particle size distribution representative of "clear" conditions together with the sky radiometry measured optical thickness $\tau_{aer} = 0.2$ The use of the fine mode aerosol was justified by a fairly sharp decrease in aerosol optical depth as a function of wavelength resulting in an angstrom coefficient $\gamma = -1.6$. The comparisons between measurements and theoretical results for a single scattering model are given in Figure (9) for 19 February 2005. This shows G_{imp} as a function of the solar zenith angle for a day where PWV variation between morning and afternoon was not significant. Reasonably good agreement is seen between the theory and observations. Very similar results were obtained on other low PWV variation days (1, 2 February 2005). In comparison, we also plot the improvement factor that would be observed in a clear sky from the Rayleigh scattering alone is given by,

$$G_{imp}^{Ray} = \sqrt{1 + \sec^2(\theta_s)} \tag{9}$$

which is obtained by combining Eq. (4) and Eq. (8). It is clear that G_{imp} is significantly affected by the impact of even fairly low levels of aerosols.

5.2 Asymmetric data set

To understand how it may be possible to provide a cohesive explanation for the asymmetric data, we point out that it is well known that the aerosol size and refractive index will change in a moist environment (high RH) because water in the air condenses onto the aerosol. The growth in particle size due to the condensation of water vapor can be described as: [16]

$$r(a_w) = r_o * \left[1 + \rho \frac{m_w(a_w)}{m_o}\right]^{\frac{1}{3}} \tag{10}$$

where the water activity a_w of a soluble aerosol at radius $r(\mu m)$ can be expressed as

$$a_w = RH \exp\left[\frac{2\sigma V_w}{R_w T} \frac{1}{r(a_w)}\right] \tag{11}$$

where r_o is the dry particle radius, ρ is the particle density relative to that of water, $m_w(a_w)$ is the mass of condensed water, m_o is the dry particle mass, RH is the relative humidity, σ is the surface tension on the wet surface, V_w is the specific volume of water, R_w is the gas constant for water vapor, and T is the absolute temperature [K]. The refractive index for the wet aerosol particle (n_{eff}), modified by the increased size is simply the volume weighted average of the refractive indices of the dry aerosol substance (n_o) and the water (n_w) as :

$$n_{eff} = n_w + (n_o - n_w)\left[\frac{r_o}{r(a_w)}\right]^3 \tag{12}$$

From these formulas we note that the magnitude of the particle growth and the change of refractive index with increasing RH depends on the size r_o of the dry aerosol. Also, the magnitude of the particle growth and the change of refractive index with increasing RH (and therefore total PWV) depends on the aerosol type because the water uptake [the ratio $m_w(a_w)/m_o$ in Eq. (10)] depends on the aerosol type [16-19]. The relationship between the equivalent radius (*r),* and the relative humidity (*RH)* at different values of the equivalent radius $r_{o,}$ in the dry state, has been computed for different models by Hanel. [16] In particular, for values of RH (< 99%), the value of the ratio r/r_o are reasonably independent of r_o, and, the smaller the value of the dry state equivalent radius r_o the larger the ratio $r/r_{o.}$ In Figure 10, we plot the surface level RH measurements from our rooftop weather station [12] for 23 February 2005. We see in particular that the RH for the morning was ~ 70% while by afternoon it decreased to 30%. In Figure 11, the aerosol hydration model [16] is plotted and shows that the observed change in the RH leads to an estimated change in the radius ratio of 20%. This modification can significantly change the effective index through Eq. (12) and modify the resulting optical depth.

Since the aerosol growth is only weakly dependant on aerosol model for modest RH, we may assume that the "dry" aerosol mode is given by an urban accumulation mode, which we take to be a log-normal particle size distribution (PSD) with average radius $r_o \approx 0.15\mu m$, and the refractive index of $n_O = 1.5 - 0.2i$ [20]. In our calculations, we used the dry (low humidity) conditions observed in the afternoon of that day as a reference level. From the sun-photometer, the optical depth for the afternoon was found to be approximately $\tau_{aer} = 0.09 \approx 0.1$. Using this data, we then determine the appropriate particle size and wet aerosol particle n_{eff} by sweeping

over all possible effective particle sizes and refractive indices as determined by Eq. (12) and matching the resultant optical depth to the sun-photometer measurements. The results are plotted in Figure 12 and show that to match the optical depth $\tau_{aer} = 0.16$, the final effective radius is given as: $r(a_w) \approx 0.18\mu m$. Once the microphysical properties were estimated, we again utilize the single scattering analysis to estimate the SNR improvement. Comparisons between measurements and theoretical results for the single scattering model for these microphysical properties are given in Figure 13. We see that reasonable agreement is obtained between this simplified theoretical approach and the experimental observations.

6. SNR improvement azimuthal dependence

Within the single scattering theory, the polarization orientation at which the minimum P_b occurs should equal the azimuth angle of the sun (see Figure 1). To validate this result, the polarizer rotation angle was tracked (by rotating the detector analyzer) over several seasons since February 2004 and compared with the azimuth angle calculated using the U.S. Naval Observatory standard solar position calculator[21] (14 April 2005). As expected, the polarizer rotation angle needed to achieve a minimum P_b closely tracks the azimuth angle as shown in Figure 14. This relationship is important since it allows us to conceive of an automated approach that makes use of a precalculated solar azimuth angle as a function of time and date to automatically rotate and set both the transmitted lidar polarization and the detector polarizer at the orientations needed to minimize P_b. With an appropriate control system, it would then be possible to track the minimum P_b by rotating the detector analyzer and the transmission polarizer

simultaneously to maximize the SNR, achieving the same results as would be done manually as described above. Plans are underway to integrate this automated approach into our lidar system.

It is also useful to examine the potential impact of the polarization discrimination scheme on non-vertically pointing lidars. Typically, scanning lidars operating in an elastic or Raman backscatter mode, and are used to scan for particulates or trace constituents in the troposphere. They are of particular interest to air quality monitoring applications where it is often desired to obtain information on spatial distributions of particulates and trace constituents above an urban area This would include horizontal and near horizontal scans, e.g. along urban canyons etc. Eye safety concerns severely limit acceptable visible lidar pulse energies for these applications, so any schemes to improve received SNR's are important. As seen earlier, for a vertically pointing lidar, the SNR improvement is greatest when the sun elevation is low which restricts the period of improvement to relatively short times in the early morning and late afternoon. The situation is quite different for a non-vertical scanning lidar. To illustrate, we consider a scanning lidar located at CCNY that is designed to scan the atmosphere above the downtown New York Metropolitan skyline. Since CCNY is approximately 5 km north of the downtown area, the lidar azimuth angle does not need to vary appreciably ($\pm 15^{\circ}$) and the lidar zenith angle need only vary from $50^{\circ} \le \theta_{lid} \le 80^{\circ}$ corresponding to relatively complete coverage through the planetary boundary layer. Under these conditions, we can calculate the resultant scattering angle as a function of the observation time. From the vertical lidar results (see fig. 13), we note that significant SNR improvement only occurs for scattering angles θ_{scat} above 70 degrees. This result, when applied to the scanning geometry and making use of the symmetry of the scattering phase function, shows that significant SNR improvement will occur in the interval $70 < \Theta_{scat} < 110$. To illustrate the differences between the vertical and scanning case, we plot

in Figure 15, the variation in scattering angle for both the scanning and vertical configurations for June 21, a typically important time of the year for lidar measurements because of the increase in aerosol particulates in summer months. The scattering angle and the complete solar position (zenith and azimuth) needed to obtain it, were again calculated using the solar position calculator[21]. Figure 15 shows that for a good portion of the day (10:00 AM– 2:00 PM), the scattering angle will lie in the range $70 < \Theta_{scat} < 110$ permitting significant SNR improvement to be obtained by polarization discrimination. This is in contrast to the situation for a vertically pointing lidar (lidar zenith angle = 0) where these improvements occur for very limited times near sunrise and sunset.

We have also examined, in a very preliminary manner, the impact of multiple scattering on the polarization discrimination technique. While it is intuitive that the maximum noise suppression should occur when the receiver polarization is parallel to the scattering plane in the single scattering regime, it is not so clear that this will hold for multiple scattering. However, it can be seen in Figure 16 that even for high optical depth (multiple scattering regime $\tau_{aer} = 0.5$), the maximum noise improvement factor calculated using a full polarized RT code developed at NASA GISS [22] occurs when the differential azimuth angle is zero (i.e. the scattering plane and the observation plane are the same). Note also that when there is a 45 degree mismatch between the planes, only the minimum improvement of $\sqrt{2}$ is obtained since both polarization components are equal and the background noise is effectively unpolarized.

7. Conclusions and Summary

SNR improvements obtained from lidar backscatter measurements, using the polarization selection/tracking scheme to reduce the sky background component, can significantly increase the far range SNR as compared to un-polarized detection. This is equivalent to improvements in effective lidar range of over 30% for a SNR threshold of 10. The improvement is largest for large scattering angles, which for vertical pointing lidars occur near sunrise/sunset. It was also demonstrated that when the technique is applied to non-vertical scanning lidars, the time period under which significant SNR improvement can occur extends over a significant portion of the midday (10 AM-2 PM) thereby extending the utility of the technique. A theoretical model that simulates the background skylight within the single scattering approximation was developed and showed fairly accurate predictions of the SNR improvement factor. Asymmetric skylight reduction was sometimes observed in experimental results and is explained by the measured increase in PWV and subsequent modification of aerosol optical depth by dehydration from morning to afternoon. Finally, since the polarization axis follows the solar azimuth angle even for high aerosol loading as demonstrated using radiative transfer simulations, it is quite conceivable to automate this procedure simply by using solar position calculators to orient the polarization axes.

In all previous discussions, clear sky conditions were assumed. The impact of clouds being in the lidar field of view is more complex. From intuitive considerations, it can be conjectured that on a partially sunny day, a lidar viewing directly scattered sunlight from a cloud, with large single scattering components, will see a significant polarized light component in the detected radiation. Under those circumstances, which apply primarily to the scanning lidar

orientations, polarization discrimination should improve the SNR. However, in other circumstances such as a complete overcast sky, the background is dominated by multiple scattered light which is depolarized so the technique is probably much less useful. Clearly, more detailed examinations are needed to quantify the affects of multiple scattering by both dry and hydrated aerosols as well as clouds.

Acknowledgements

This work was partially supported under contracts from NOAA # NA17AE1625 and NASA # NCC-1-03009.

References

1. R. M. Schotland, K. Sassen, and R. J. Stone, "Observations by lidar of linear depolarization ratios by hydrometeors," *J. Appl. Meteorol.* **10,** 1011–1017 (1971).

2. K. Sassen, "Depolarization of laser light backscattered by artificial clouds," *J. Appl. Meterol*. **13,** 923–933 (1974).

3. C. M. R. Platt, "Lidar observation of a mixed-phase altostratus cloud," *J. Appl. Meteorol.* **16,** 339–345 (1977).

4. K. Sassen, "Scattering of polarized laser light by water droplet, mixed-phase and ice crystal clouds. 2. Angular depolarization and multiple scatter behavior," *J. Atmos. Sci*. **36,** 852–861 (1979).

5. C. M. R. Platt, "Transmission and reflectivity of ice clouds by active probing," in *Clouds, Their Formation, Optical Properties, and Effects*, P. V. Hobbs, ed. Academic, San Diego, Calif., 407–436 (1981).

6. Kokkinos, D. S., Ahmed, S. A. "Atmospheric depolarization of lidar backscatter signals" *Lasers '88; Proceedings of the International Conference*, Lake Tahoe, NV, (A90-30956 12-36, McLean, VA, STS Press, 1989), pp. 538-545.

7. G.P.Gobbi, “Polarization lidar returns from aerosols and thin clouds: a framework for the analysis,” *Appl. Opt.* **37,** 5505-5508 (1998).

8. N. Roy, G. Roy, L. R. Bissonnette, and J. Simard, ”Measurement of the azimuthal dependence of cross-polarized lidar returns and its relation to optical depth,” *Appl. Opt.* **43,** 2777-2785 (2004).

9. J. Hansen, and L. Travis, “Light Scattering in Planetary Atmospheres,“ *Space Science Reviews* **16,** 527-610 (1974).

10. Yasser Y. Hassebo, B. Gross, F. Moshary, Y. Zhao, S. Ahmed “Polarization discrimination technique to maximize LIDAR signal-to-noise ratio” in *Polarization Science and Remote Sensing II*, Joseph A. Shaw, J. Scott Tyo, eds., Proc. SPIE **5888**, 93-101 (2005).

11. Yasser Y. Hassebo, Barry M. Gross, Min M. Oo, Fred Moshary, Samir A. Ahmed “Impact on lidar system parameters of polarization selection / tracking scheme to reduce daylight noise” *in Lidar Technologies, Techniques, and Measurements for Atmospheric Remote Sensing*, Upendra N. Singh, ed., Proc. SPIE **5984,** 53-64 (2005).

12. NOAA-CREST webpage: http://earth.engr.ccny.cuny.edu/noaa/wc/DailyData/

13. M.V. Klein, *Optics* (Wiley, New York, 1970).

14. R. M. Measures, *Laser Remote Sensing* (Wiley, New York, 1984).

15. K.N. Liou, *An Introduction to Atmospheric Radiation* (Academic Press, California, 2002).

16. G. Hanel, "The properties of atmospheric aerosol particles as functions of the relative humidity at thermodynamic equilibrium with the surrounding moist air," *Advances in Geophysics*, H. E. Landsberg and J. Van Mieghem, eds. Academic, New York **19,** 73–188 (1976).

17. P. V. N. Nair and K. G. Vohra, "Growth of aqueous sulfuric acid droplets as function of relative humidity," *J. Aerosol Sci*. **6,** 265–271 (1975).

18. G. Hanel and M. Lehmann, "Equilibrium size of aerosol particles and relative humidity: new experimental data from various aerosol types and their treatment for cloud physics application," *Contr. Atmos. Phys*. **54**, 57-71 (1981).

19. B. Yan, K. Stamnes, W. Li, B. Chen, J. J. Stamnes and S-C Tsay "Pitfalls in atmospheric correction of ocean colorimagery: how should aerosol optical propertiesbe computed?" *Appl. Opt.* **41,** 412- 423 (2002).

20. E. P Shettle and R. W. Fenn,: *Models of the Aerosols of the Lower Atmosphere and the Effects of Humidity Variations on their Optical Properties*. Project 7670, Air Force Geoph. Lab., Massachusetts (1979)

21. Solar Calculator Webpage: http://aa.usno.navy.mil/data/docs/AltAz.html

22. J. Chowdhary, B. Cairns, L.D. Travis, "The contribution of the water leaving radiances to multiangle, multispectral polarimetric observations over the open ocean: Bio-optical model results for Case I waters". To appear: Special Issue "Polarization Imaging and Remote Sensing" Appl. Opt. (2006).

Captions

Figure 1: Sky background suppression geometry for a vertical pointing lidar: θ_s is the solar zenith angle (equal to the scattering angle for this geometry) ϕ_s is the solar azimuth angle; and OAB is the solar scattering plane

Figure 2: Schematic diagram of polarization experiment set up for elastic biaxial monostatic lidar (mobile lidar system)

Figure 3: Comparison of max P_b verses min P_b lidar signals at 6:29 PM on 07 October 2004.

Figure 4: Comparison of experimental return signals at 6:29 PM, 3 PM and noon on 07 October 2004, Range of 20- 30 km, both orthogonal cases are shown.

Figure 5: Experimental range dependent SNR for maximum and minimum polarization orientations

Figure 6(a): G_{imp} in detection wavelength of 532 nm verses local time on 19 February 2005

Figure 6(b): G_{imp} in detection wavelength of 532 nm verses solar zenith angle on 19 February 2005

Figure 7: G_{imp} in detection wavelength of 532 nm verses solar zenith angle on 23 February 23 2005

Figure 8: PWV (cm) loading verses local time on 19 February 2005 and 23 February 2005

Figure 9: Theoretical model agrees with experimental measurements: 19 February 2005 Rayleigh scattering alone is also shown

Figure 10: Relative humidity, *RH*, verses local time of New York City on 23 February 2005

Figure 11: The particle equivalent radius ratio r/ r_o verses relative humidity, *RH*, at different equivalent radius, r_o, in the dry stat (*RH = 0*), and for two aerosol models at 20º C temperature [19].

Figure 12: Theoretical model: 23 February 2005

Figure 13: Theoretical model agrees with experimental measurements: 23 February 23 2005

Figure 14: Comparison between solar azimuth angle and angle of polarization rotation needed to achieve minimum P_b: 14 April 2005

Figure 15: The scattering angle between the solar and lidar directions for the scanning lidar geometry as function of lidar zenith angle and time of day showing time period where SNR improvement can be significant. The vertical lidar result is also plotted to contrast the time periods.

Figure 16: Multiple scattering model showing the minimum noise is parallel to the scattering plane irregardless of OD

Table I: Lidar system specifications

Table II: Comparison of experimental results to verify shot noise operation

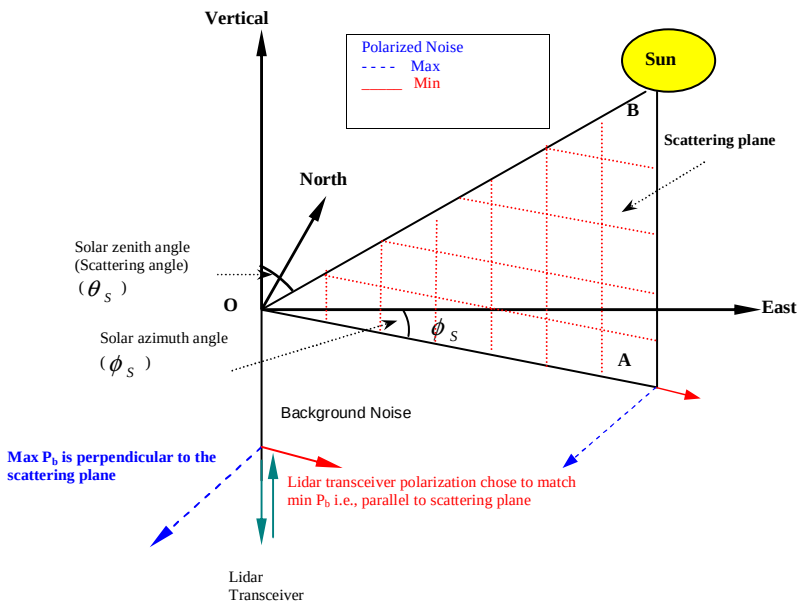

Figure 1: Sky background suppression geometry for a vertical pointing lidar: θ_s is the solar zenith angle (equal to the scattering angle for this geometry) ϕ_s is the solar azimuth angle; and OAB is the solar scattering plane

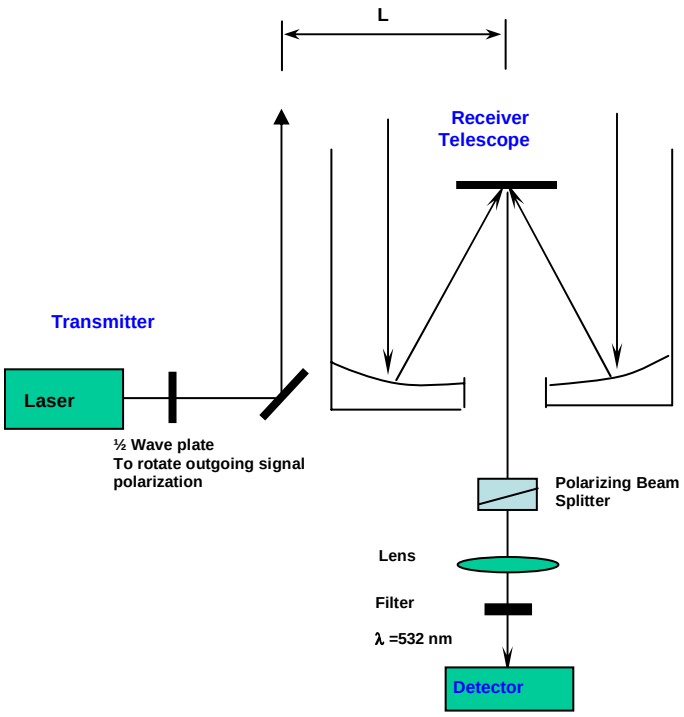

Figure 2: Schematic diagram of polarization experiment set up for elastic biaxial monostatic lidar (mobile lidar system)

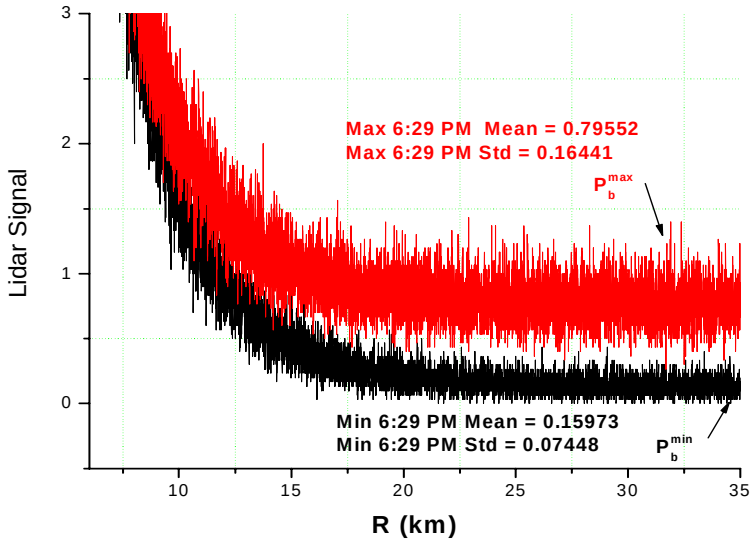

Figure 3: Comparison of max P_b verses min P_b lidar signals at 6:29 PM on 07 October 2004.

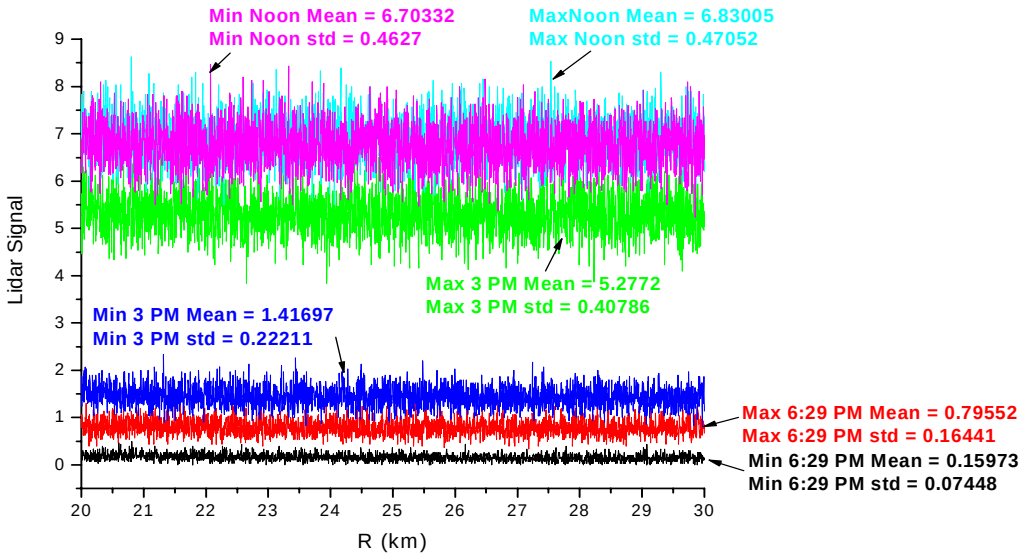

Figure 4: Comparison of experimental return signals at 6:29 PM, 3 PM and noon on 07 October 2004, range of 20- 30 km, both orthogonal cases are shown.

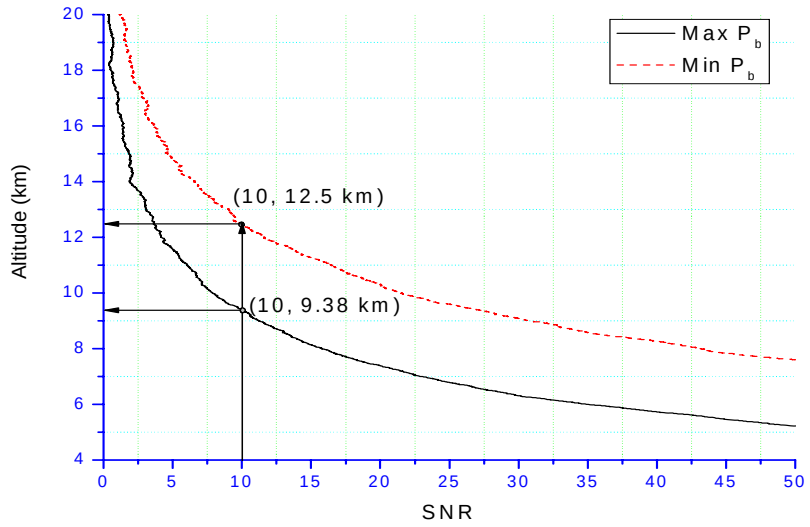

Figure 5: Experimental range dependent SNR for maximum and minimum polarization orientations

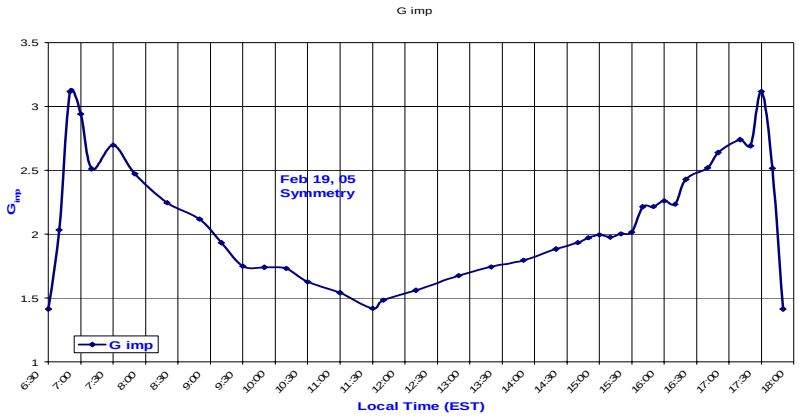

Figure 6(a): G_{imp} in detection wavelength of 532 nm verses local time on 19 February 2005

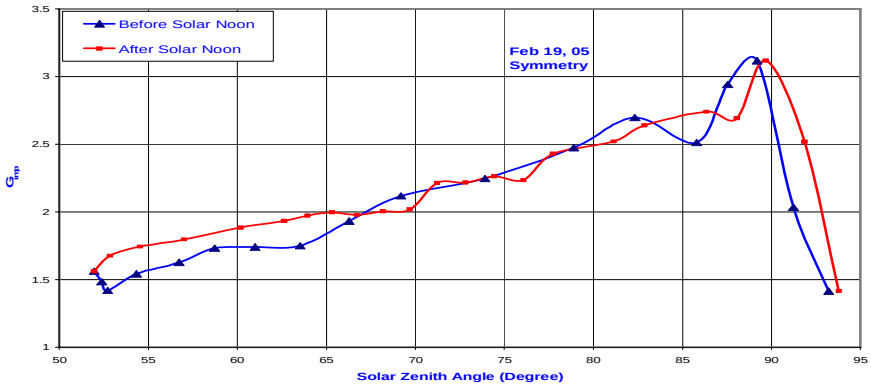

Figure 6(b): G_{imp} in detection wavelength of 532 nm verses solar zenith angle on 19 February 2005

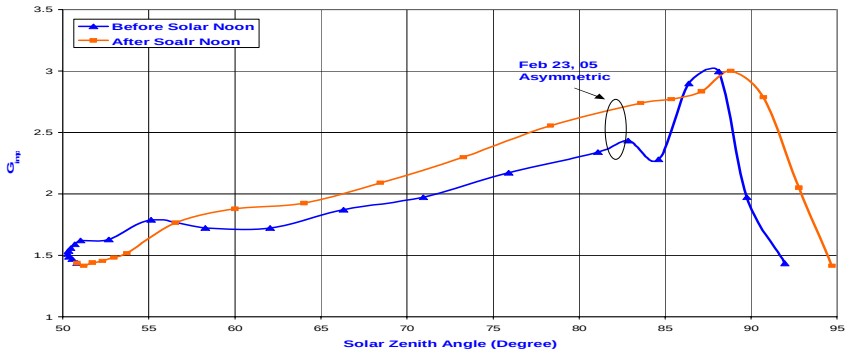

Figure 7: G_{imp} in detection wavelength of 532 nm verses solar zenith angle on 23 February 2005

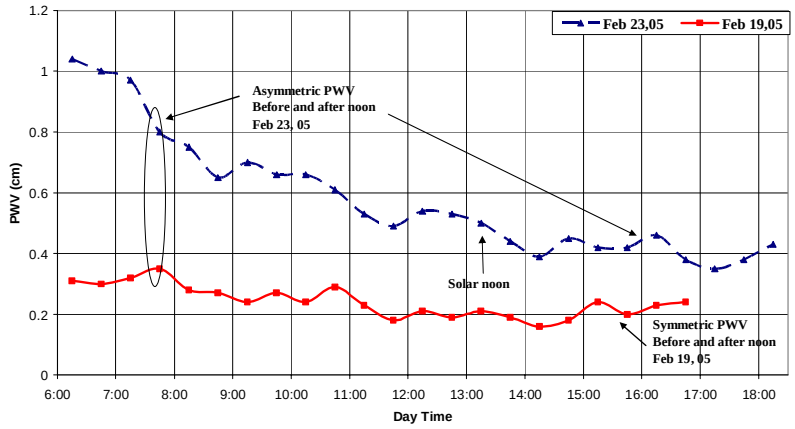

Figure 8: PWV (cm) loading verses local time on 19 February 2005 and 23 February 2005

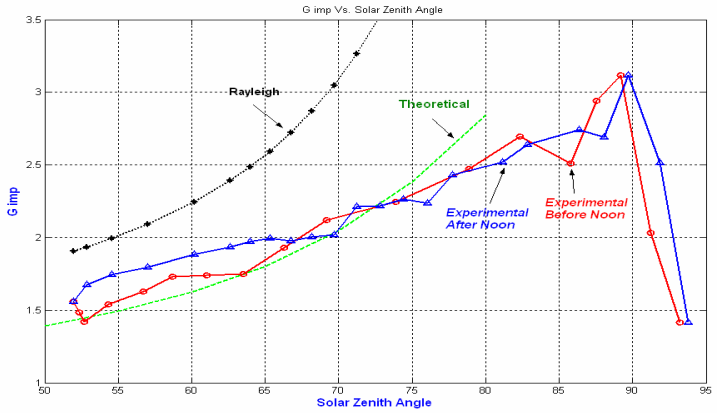

Figure 9: Theoretical model agrees with experimental measurements: 19 February 2005

Rayleigh scattering alone is also shown

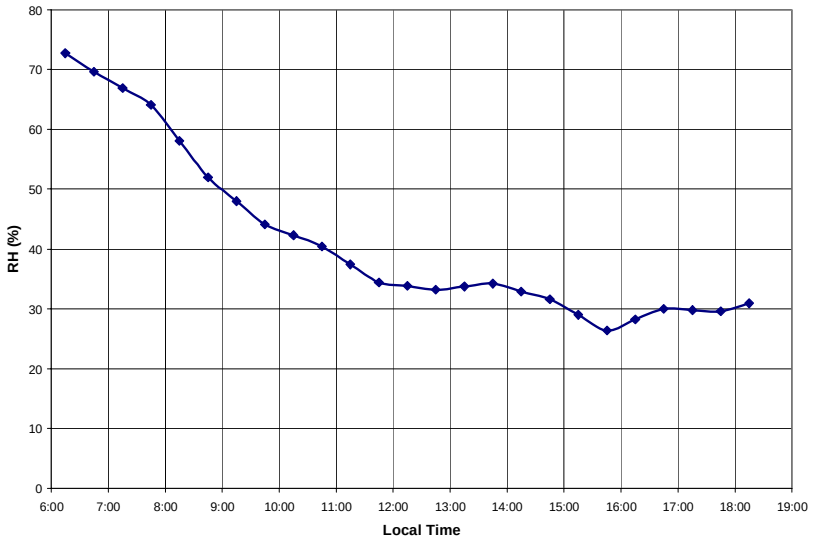

Figure 10: Relative humidity, *RH*, verses local time of New York City on 23 February 2005

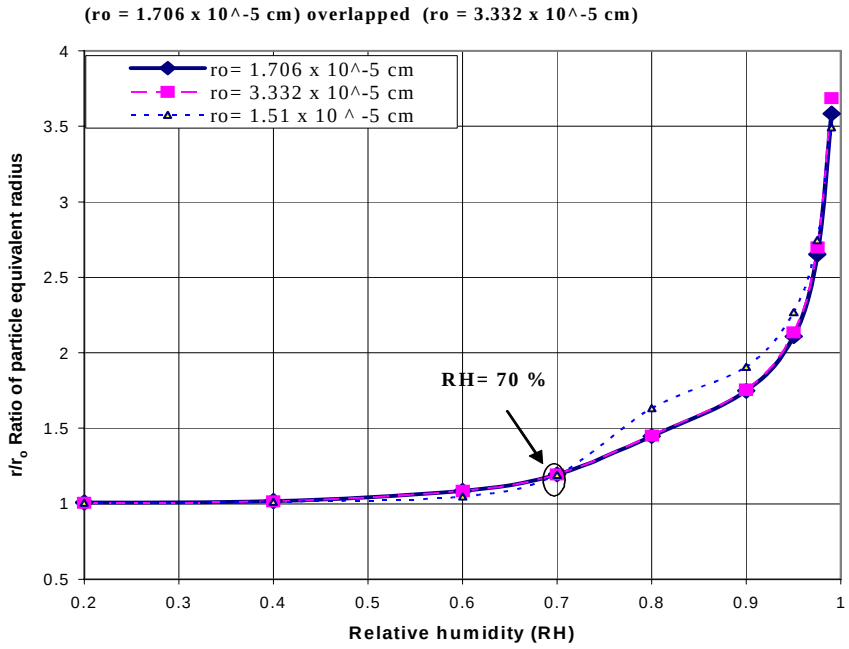

Figure 11: The particle equivalent radius ratio r/ r_o verses relative humidity, *RH*, at different equivalent radius, $r_{o,}$ in the dry state (*RH = 0*), and for two aerosol models at 20º C temperature [19].

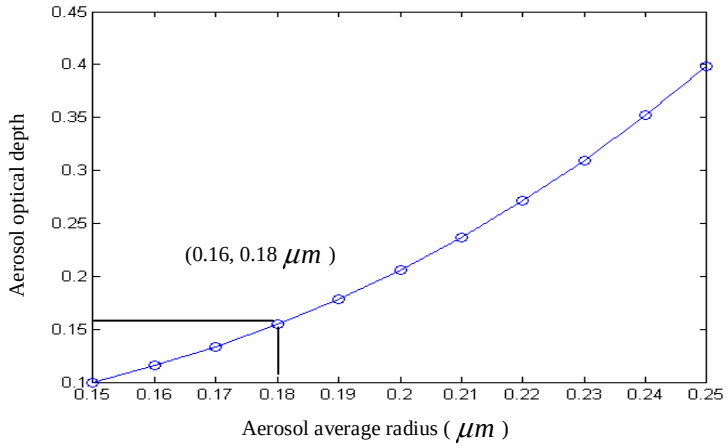

Figure 12: Theoretical model: 23 February 2005

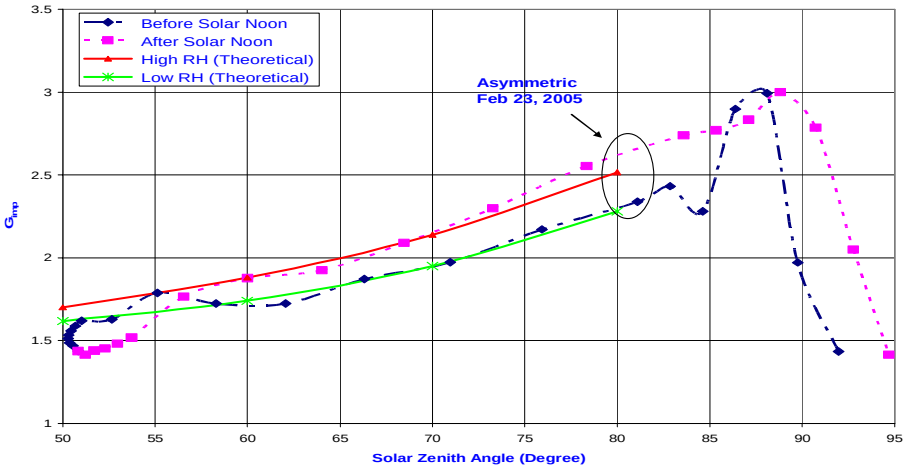

Figure 13: Theoretical model agrees with experimental measurements: 23 February 2005

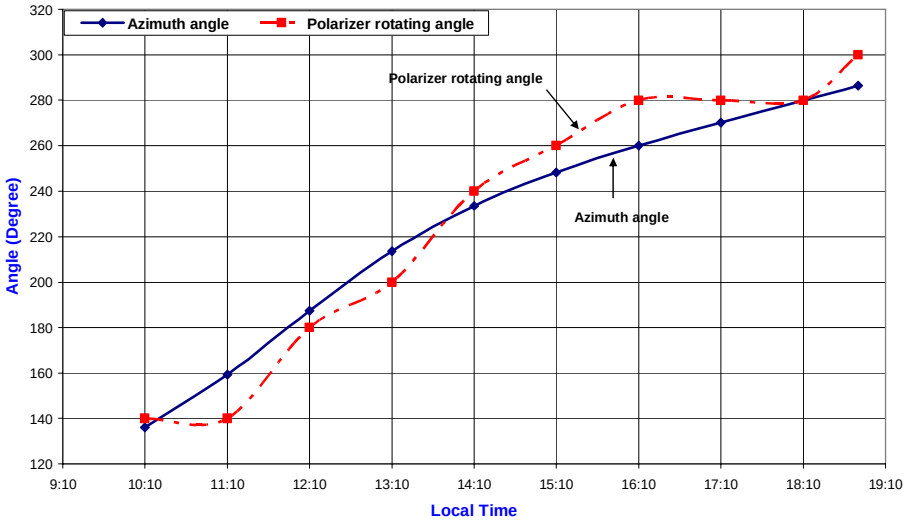

Figure 14: Comparison between solar azimuth angle and angle of polarization rotation needed to achieve minimum P_b: 14 April 2005

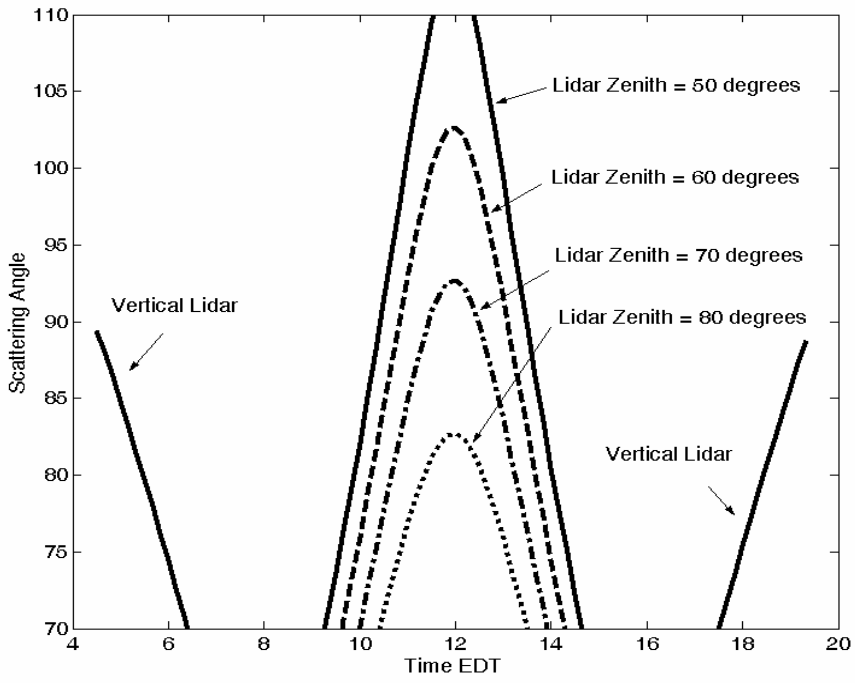

Figure 15: The scattering angle between the solar and lidar directions for the scanning lidar geometry as function of lidar zenith angle and time of day showing time period where SNR improvement can be significant. The vertical lidar result is also plotted to contrast the time periods.

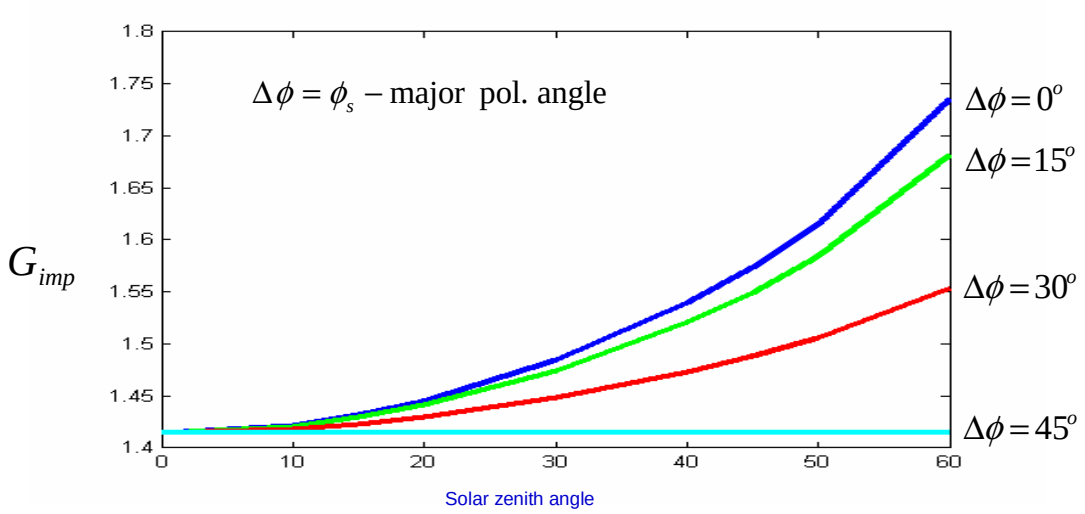

Figure 16: Multiple scattering model showing the minimum noise is parallel to the scattering plane irregardless of OD

Table I: Lidar system specifications

Transmitter			**Receiver**	
Laser	Q-Switched Nd: YAG Continuum Surelite ll - 10		**Telescope Aperture**	CM_1400 Schmidt Cassegrian telescope 35.56 mm
Wavelength	1064, 532, 355 nm		**Focal length**	3910 mm
Energy/pulse	650 mj at 1064 nm 300 mj at 532 nm 100 mj at 355 nm		**Detectors** **532 nm** **355 nm** **1064 nm**	Hamamatsu PMT: R11527 P PMT: R758-10 APD
Pulse Duration	7 ns at 1064 nm		**Data Acquisition**	LICEL TR 40-160
Repetition Rate	10 Hz		**Photon Counting**	LICEL TR 40-160
Harmonic Generation	Surelite Double (SLD) Surelite Third Harmonic (SLF)			

Table II: Comparison of experimental results to verify shot noise operation ($\Delta R = \sqrt{R}$)

Time	$\Delta P_{\min}$	$\langle P_{\min} \rangle$	$\Delta P_{\max}$	$\langle P_{\max} \rangle$	$R = \frac{\langle P_{\max} \rangle}{\langle P_{\min} \rangle}$	$\Delta R = \frac{\Delta P_{\max}}{\Delta P_{\min}}$	$\sqrt{R}$
Noon	0.46	6.7	0.47	6.83	1.2	**1.019**	**1.09**
3:00 PM	0.22	1.41	0.40	5.27	3.72	**1.82**	**1.9**
6:29 PM	0.074	0.159	0.164	0.795	5.2	**2.2**	**2.2**